

Micro-PIV simulation and measurement in complex microchannel geometries

M R Bown, J M MacInnes and R W K Allen

Department of Chemical and Process Engineering, University of Sheffield, Newcastle Street, Sheffield, S1 3JD, UK

E-mail: m.bown@sheffield.ac.uk

Received 29 July 2004, in final form 22 October 2004

Published 31 January 2005

Online at stacks.iop.org/MST/16/619

Abstract

Using low numerical aperture lenses to achieve a large field of view when carrying out micron resolution particle image velocimetry (micro-PIV) experiments may result in the out-of-plane resolution being a significant fraction of the overall channel depth. A method to estimate the effect of out-of-plane resolution on micro-PIV velocity measurements is applied to two microchannel flows: a two-dimensional developed flow in a straight channel and a three-dimensional periodic flow in a ribbed channel. The method combines numerical simulation based on computational fluid dynamics (CFD) with an approximation for the contribution to the correlation function arising from partially defocused particles. The flows are then investigated experimentally with measurements obtained on a number of evenly spaced planes. The dominating factor in the comparison between the micro-PIV results and CFD simulations is not the spatial resolution of the experimental data, but instead the precision with which the geometrical parameters can be determined. A methodology is also presented for using micro-PIV results to measure the depth of microfluidic devices. Parabolic fitting of flow profiles allows the top and bottom surfaces of the channel to be located to within $0.2 \mu\text{m}$.

Keywords: micron resolution particle image velocimetry, microfluidics, spatial resolution

1. Introduction

Micron resolution particle image velocimetry (micro-PIV) measurements have been carried out in a range of flow geometries including straight channels [1, 2], an inkjet printer head [3], around a human blood cell [4], a micro-cell sorter [5] and a non-moving part valve [6]. In general the accuracy of these measurements is increased by improving the spatial resolution. This is defined as the size of the base interrogation spot in the image plane and the depth over which particles contribute significantly to the cross-correlation perpendicular to the plane. This definition of out-of-plane resolution arises from the volume illumination that is usually used in micro-PIV applications. Theoretical studies have investigated the limit placed on the in-plane resolution by diffraction [7] and have defined parameters such as the measurement depth [8] and the depth of correlation [9]

to describe the out-of-plane resolution. The depth of correlation has been extended to include the effects of out-of-plane Brownian motion [10] and out-of-plane velocities [11] and has recently been demonstrated experimentally and computationally [12]. The errors associated with the micro-PIV technique have also been investigated, in particular the effect of Brownian motion [13] and the error in locating the particle image and correlation function centres [14].

In many practical cases, however, it may not be possible to limit the spatial resolution. This is particularly true for the out-of-plane resolution, which is reduced by decreasing the ratio of n to numerical aperture (NA), where n is the index of refraction of the immersion medium [7]. This will usually coincide with an increase in magnification and a reduction in field of view, which may be undesirable. In addition, high quality optical access will usually be required for the use of high NA lenses, which may not be possible in many practical devices.

Flows with significant out-of-plane velocities may also cause problems as particles will become defocused between the base and cross images if the depth of correlation is small.

In this work micro-PIV studies are carried out in two microchannel geometries, which have moderate optical access and require a large field of view. Thus lenses with relatively low magnification and NA are required. The first is an isotropically etched straight channel, whilst the second is a more complex flow geometry with 45° ribs running across the roof of the channel to create a three-dimensional flow field. Both of the flows occur at low Reynolds number and can readily be computed using computational fluid dynamics (CFD). Relations developed to represent the depth of correlation [9, 11] are applied to the CFD results to look at the magnitude of the error in velocity due to the moderate spatial resolution arising from the low NA lenses. This is compared to the magnitude of the other sources of experimental error.

Accurate measurement of the depth of channels is difficult. A straightforward technique is to focus by eye on particles attached to the top and bottom surfaces [15]. Micro-PIV has been used to measure the positions of channel walls by determining the point at which the results no longer conform to the known flow profile [16]. Here, data from several measurement planes are fitted to the known velocity profile to improve the measurement of the depth dimension for the microchannel devices considered.

2. Experimental details

The details of the micro-PIV technique are described elsewhere [2]. In this study the experimental data were obtained using an Oxford Lasers Micro-PIV system built around a Zeiss Axiovert S100 microscope with a Zeiss Achroplan lens ($M = 20$, $NA = 0.4$). Flows were seeded with $1 \mu\text{m}$ diameter polystyrene particles ($\rho_p = 1005 \text{ kg m}^{-3}$). When excited with an Nd:YAg laser ($\lambda = 532 \text{ nm}$) the particles fluoresce at around 585 nm and their images are captured on a CCD array (PCO Sensicam). Analysis of the images was carried out using in-house micro-PIV software written in MATLAB. The software allows arithmetic and geometric correlation function averaging to improve the signal-to-noise ratio [2] and larger spots on the cross image to remove velocity biasing [17]. The use of non-square interrogation spots and knowledge about the flow direction allows the resolution to be optimized.

The straight microchannel used was isotropically-etched in glass using hydrofluoric acid, resulting in a D-shaped profile of width $W = 262.7 \mu\text{m}$ and depth $R = 73.3 \mu\text{m}$ similar to that described by MacInnes *et al* [15]. The pressure gradient along it was controlled by altering the levels in large reservoirs connected to the inlet and outlet. Velocities are normalized with the average velocity and dimensions with the channel depth R . The geometry and coordinate system are shown in figure 1.

The geometry of the ribbed channel is shown in figure 2. The actual channel was produced by interference etching from a series of closely spaced, slanted mask lines. The ribs result from the overlap of the etched grooves from adjacent lines. Sufficient etching time must be allowed for the grooves to join to form a channel, but not so long that the ribs are etched

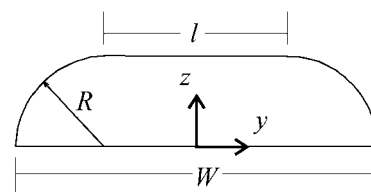


Figure 1. Design geometry of the wet-etched, straight microchannel. The geometry is completely defined by the two parameters R and $l = W - 2R$ shown.

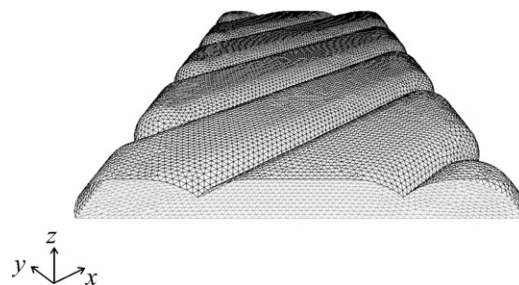


Figure 2. Ribbed microchannel geometry resulting from an ideal interference etch. The geometry consists of overlapping cuboidal, cylindrical and spherical sections. The channel repeats periodically, four periods are shown here.

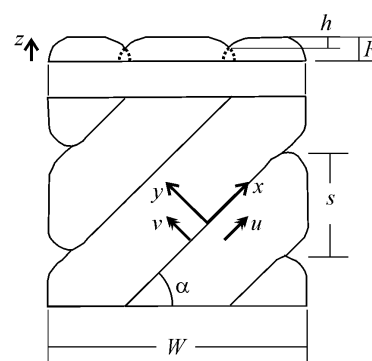


Figure 3. Design geometry of the ribbed microchannel. The geometry is completely defined by the five parameters h , R , s , α and W shown. The ribs result from overlap between the etch patterns from the adjacent grooves (dotted lines).

completely away. The geometry may be completely defined by five parameters (figure 3). The channel in this study has ribs at $\alpha = 45^\circ$, repeating periodically every $206 \mu\text{m}$. The overall channel depth, R , is $46.5 \mu\text{m}$, with $h/R = 0.45$. The overall channel width, W , is $510 \mu\text{m}$. To allow the complete width of the channel to be studied the images were taken at a 45° angle across the channel (see figure 7). In order to facilitate the analysis of the images the coordinate system is thus also oriented at 45° , such that the x direction lies along the ribs and the y direction perpendicular to the ribs. Again, the z direction is normal to the measurement plane. Velocities in the ribbed channel are normalized with the average axial velocity in an isotropically etched channel with the same W and R and dimensions are normalized with R . The fluid to be passed to the chip was contained in small ($\sim 2 \text{ ml}$) reservoirs at the inlet and pneumatic pressure was applied to the fluid surface via a nitrogen line. A regulator allows pressures from 0.1 to 5 bar to be used.

3. CFD computations

Computational solutions were obtained for the flow in both channels. Since away from the channel ends the flow in the straight channel is laminar and constant with x , it can be modelled in a 2D cross section using Poisson's equation for the streamwise velocity. This equation can be written in terms of the normalized variables as follows:

$$0 = -\frac{\partial P}{\partial x} + \left(\frac{\partial^2 u}{\partial y^2} + \frac{\partial^2 u}{\partial z^2} \right). \quad (1)$$

P is the normalized pressure. Experimental measurements were taken sufficiently far from either end of the channel for the flow profile to be fully developed. A numerical solution was obtained using the FEMLAB 2.3 code. By modelling the problem in 2D in this way grid independence of the solution can be achieved. For the ribbed channel $\partial u / \partial x \neq 0$ and a 3D computation of the Navier–Stokes and continuity equations is required. This was carried out using the Fluent 5 code. The developed flow is periodic across one rib-spacing (s in figure 3). When carrying out the experiments, a region of the channel sufficiently far from either end and away from any fabrication defects was selected so that this assumption of periodicity would be closely approximated. Grid independence studies suggest that a grid of 200 000 cells produces a solution that is accurate to within 2%. This corresponds to 10 cells across the depth of the channel with smaller cells in the vicinity of the rib passage.

4. Micro-PIV simulation

In the experiments, the correlation function is averaged across many image pairs to improve the signal-to-noise ratio. The averaging also improves convergence of the measured velocity, \mathbf{u}_{PIV} , onto the weighted average of the velocity field over the interrogation volume, $\mathbf{u}_{\text{PIV}}^*$ [9]:

$$\mathbf{u}_{\text{PIV}}^* = \frac{\int W \mathbf{u} dV}{\int W dV}. \quad (2)$$

W is a weighting function including terms for the particle image intensity distribution and biasing due to velocity variation and the integral is over the flow volume. Correlation averaging allows the in-plane resolution to be reduced until it is small compared to the length scale over which velocity variations occur. In the z direction, the interrogation volume depth is determined by the point at which the weighting function falls below some fraction ϵ [9]. Velocities outside this depth contribute negligibly to the overall average. Hence equation (2) can be rewritten in terms of ζ , the z displacement from the interrogation volume centre, as

$$\mathbf{u}_{\text{PIV}}^* = \frac{\int_{-a}^{+a} W \mathbf{u} d\zeta}{\int_{-a}^{+a} W d\zeta} \quad (3)$$

where $2a$ is the interrogation spot depth. The top and bottom parts of this equation can be expanded using a MacLaurin series and integrated term by term.

$$\mathbf{u}_{\text{PIV}}^* = \left(2a(W\mathbf{u})|_0 + \frac{\partial(W\mathbf{u})/\partial\zeta|_0}{2}(a^2 - a^2) + \frac{2\partial^2(W\mathbf{u})/\partial\zeta^2|_0}{3!}a^3 + \dots \right)$$

$$\times \left(2aW|_0 + \frac{\partial W/\partial\zeta|_0}{2}(a^2 - a^2) + \frac{2\partial^2 W/\partial\zeta^2|_0}{3!}a^3 + \dots \right)^{-1}, \quad (4)$$

where $\partial W/\partial\zeta|_0$ is the derivative evaluated at $\zeta = 0$. It can be seen that the odd derivative terms drop out of the equation and that a factor of $2a$ can be cancelled from the top and bottom parts. If the weighting function is symmetrical about the centre of the interrogation volume, then all odd derivatives of W can be set to zero. More light will be collected from particles deviating towards the lens than from particles that deviate away from the lens. However, since the lens object distance $s_0 \gg \zeta$, the resulting asymmetry in the weighting function can be neglected. Expanding the derivatives of Wu and writing the result as an infinite series results in the following expression for $\mathbf{u}_{\text{PIV}}^*$:

$$\mathbf{u}_{\text{PIV}}^* = \sum_{m=0}^{\infty} \left[\frac{\partial^{2m} \mathbf{u}}{\partial \zeta^{2m}} \Big|_0 \left(\sum_{n=m}^{\infty} \frac{{}^{2n}C_{2m}}{(2n+1)!} a^{2n} \frac{\partial^{2(n-m)} W}{\partial \zeta^{2(n-m)}} \Big|_0 \right) \times \left(\sum_{n=0}^{\infty} \frac{1}{(2n+1)!} a^{2n} \frac{\partial^{2n} W}{\partial \zeta^{2n}} \Big|_0 \right)^{-1} \right] \quad (5)$$

where C represents the combination operator, i.e. ${}^{2n}C_{2m} = (2n)!/(2m)!(2n-2m)!$. The first term in the above equation ($m = 0$) is \mathbf{u}_0 , the velocity at the centre of the interrogation volume. Velocity derivatives of order greater than 2 can be dropped from the equation. For parabolic velocity profiles this is exact, whilst for other flows it will often be an excellent approximation. Thus, equation (5) can be simplified to give the following relation between $\mathbf{u}_{\text{PIV}}^*$ and \mathbf{u}_0 :

$$\mathbf{u}_{\text{PIV}}^* = \mathbf{u}_0 + a^2 \frac{\partial^2 \mathbf{u}}{\partial \zeta^2} \Big|_0 \left(\sum_{n=1}^{\infty} \frac{{}^{2n}C_2}{(2n+1)!} a^{2(n-1)} \frac{\partial^{2(n-2)} W}{\partial \zeta^{2(n-2)}} \Big|_0 \right) \times \left(\sum_{n=0}^{\infty} \frac{1}{(2n+1)!} a^{2n} \frac{\partial^{2n} W}{\partial \zeta^{2n}} \Big|_0 \right)^{-1}. \quad (6)$$

The infinite sums are constants for any particular W so the difference between $\mathbf{u}_{\text{PIV}}^*$ and \mathbf{u}_0 is proportional to the second derivative of the velocity field. The size of the interrogation spot can be estimated using parameters such as the depth of correlation [9] or the measurement depth [8].

In order to estimate $\mathbf{u}_{\text{PIV}}^*$ an expression for the weighting function is required. Olsen and Adrian [9] propose an expression for W , assuming that velocity variations within an interrogation volume are small. This is extended to include the effect of out-of-plane velocities by Olsen and Bourdon [11] to give the expression

$$W(\mathbf{x}) = \frac{C(\mathbf{x}, t) W_1(M\mathbf{x} - \mathbf{X}_1) W_2(M(\mathbf{x} + \Delta\mathbf{x}) - \mathbf{X}_2)}{(s_0 + \zeta)^2 (s_0 + \zeta + \Delta\zeta)^2 (d_e^2(\zeta) + d_e^2(\zeta + \Delta\zeta))^2} \quad (7)$$

where C is the average concentration, the W_1 are window functions representing the interrogation volumes, s_0 is the lens–object distance and d_e is the particle image diameter. The \mathbf{X} are the interrogation volume centres, and $\Delta\zeta$ is the vertical displacement of the particle between the base and cross images. Note that this equation could be written in exactly the same form in terms of the absolute position z , instead of ζ . Since the average concentration can be taken as constant it will cancel on the top and bottom of

equation (2). Also, by using a larger interrogation spot on the cross images the biasing due to velocity gradients can be removed [17]. If the cross spot is sufficiently large then the product $W_{11}(M\mathbf{x} - \mathbf{X}_1)W_{12}(M(\mathbf{x} + \Delta\mathbf{x}) - \mathbf{X}_2)$ will be one everywhere inside the base interrogation volume and zero otherwise. Finally, if $s_o \gg \zeta$, equation (7) can be rewritten as

$$W(\mathbf{x}) = \frac{A}{(d_e^2(\zeta) + d_e^2(\zeta + \Delta\zeta))^2}, \quad (8)$$

where A is a normalization constant. Thus the weighting function requires an expression for the particle image diameter, d_e , as a function of distance from the measurement plane. The model proposed by Olsen and Adrian [9] and demonstrated experimentally by Bourdon *et al* [12] uses a Gaussian approximation based on a combination of geometric and simple diffraction effects resulting in the following:

$$d_e = \left(M^2 d_p^2 + M^2 \left(\frac{\zeta}{\zeta + s_o} \right)^2 D_a^2 + 5.95(M+1)^2 \lambda^2 f^{\#2} \right)^{\frac{1}{2}}. \quad (9)$$

d_p is the particle diameter, D_a is the lens diameter and $f^{\#}$ is the f -number of the lens. M is the magnification of the lens and λ is the wavelength of the light. The result is derived for a single lens, and recent work [7] suggests that the $(M+1)$ should be replaced by M for an infinity-corrected lens system, such as that used in the present work. The f -number is defined as $f^{\#} = f/D_a = 1/2 \tan \theta$. This can be combined with the definition of numerical aperture ($\text{NA} = n \sin \theta$) in one of two ways. Using the paraxial assumption ($\sin \theta \approx \tan \theta \approx \theta$), the equation for f -number becomes $f^{\#} = n/2\text{NA}$. Alternatively, the more complete trigonometric identity $\sin \theta = (1/\tan^2 \theta + 1)^{-\frac{1}{2}}$ can be used [7], resulting in

$$f^{\#} = \frac{1}{2} \left[\left(\frac{n}{\text{NA}} \right)^2 - 1 \right]^{\frac{1}{2}}, \quad (10)$$

if $(n/\text{NA})^2 \gg 1$, the two expressions agree. For the lens used in the current study $(n/\text{NA})^2 = 6.25$ and the error resulting from the paraxial approximation is around 9%. Using equation (10), the expression for d_e can be rewritten as follows:

$$d_e = M \left(d_p^2 + 4 \left[\left(\frac{n}{\text{NA}} \right)^2 - 1 \right]^{-1} \zeta^2 + 1.49 \lambda^2 \left[\left(\frac{n}{\text{NA}} \right)^2 - 1 \right]^{\frac{1}{2}} \right)^{\frac{1}{2}}. \quad (11)$$

Note that the assumption of $s_o \gg \zeta$ has again been made; this is reasonable since the lens working distance is typically a few millimetres whilst the variation in ζ is of the order 1 to 10 μm . This approximation for d_e can be used with equation (8) to compute W in either equation (6) or equation (2) and thus predict the micro-PIV velocity from CFD computations of the flow field. In this study equation (2) has been used and is implemented numerically across simulated interrogation volumes within the CFD solution. A further simplification has been made to facilitate this implementation. It has been assumed that the displacement of the particles in the z direction between the images is small enough that

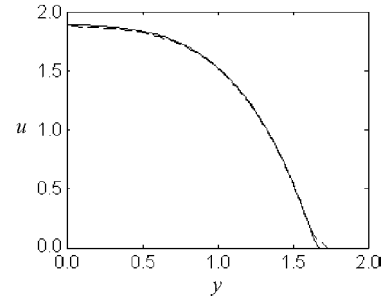


Figure 4. A comparison between the exact numerical solution, u_0 (solid), and the predicted micro-PIV result, u_{PIV}^* (dashed), at $z = 0.5$ in the straight microchannel. The maximum deviation is 0.7% in the centre of the channel, which is significant compared to the precision of the grid-independent CFD solution.

$d_e^2(\zeta) = d_e^2(\zeta + \Delta\zeta)$. This assumption is reasonable as the time between images is selected based on the in-plane velocities, which are at least an order of magnitude greater than the out-of-plane velocities for most of the flow. Thus the out-of-plane particle displacements will be small.

5. Computational results

Figure 4 compares the predicted micro-PIV velocities (u_{PIV}^*) with the computational result (u_0) on the $z = 0$ plane in the straight microchannel. The integration is over an interrogation spot of 2.6 μm across the channel, with the out-of-plane weighting function based upon the $M = 20$, $\text{NA} = 0.4$ lens used in the experiment. u_{PIV}^* lies below u_0 over most of the channel, with the maximum deviation of 0.7% of the centreline velocity occurring in the centre. This deviation is significant compared to the precision of the grid-independent CFD solution. Near the walls u_{PIV}^* is higher than u_0 and data are obtained even when the centre of the interrogation spot is no longer in the channel. For this particular case data are obtained for an additional 4.7 μm beyond the channel wall even though the spot width is only 2.6 μm . The reason for this is that the isotropically etched channel has curved walls and the depth of the interrogation volume is such that data can still be obtained from below the measurement plane, where the channel is wider.

In the ribbed channel (figure 5) the systematic deviation between u_{PIV}^* and u_0 is more pronounced. This is particularly true at the rib tip ($y = 0$) where the deviation peaks at 20% of the reference velocity, although at this point the interrogation region lies partly in the channel wall. When the interrogation spot first lies completely in the flow, $y = \pm 0.38$, the deviation is around 7.5%. These deviations are significant as a grid independence analysis suggests that the computational solutions are correct to within 2%. The simulations were again carried out for $M = 20$ and $\text{NA} = 0.4$, but this time the in-plane resolution is larger as a result of the larger spot size necessary to obtain good quality experimental data. The spot size used in both the simulation and experiment was $21.2 \times 21.2 \mu\text{m}$. Simulations made with differing spot sizes (results not shown) suggest that the in-plane resolution is not the dominant factor when determining the systematic deviation.

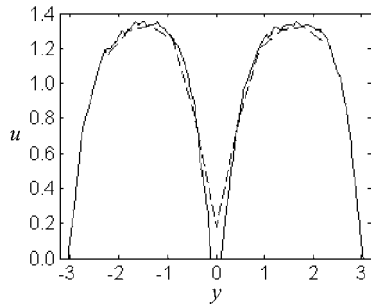


Figure 5. A comparison between u_0 (solid) and u_{PIV}^* (dashed) at $z = 0.68$ in the ribbed microchannel. The deviation is approximately 1% of the mean velocity in the centre of the grooves, rising to 7.5% at $y = \pm 0.38$ and 20% at $y = 0$, when much of the interrogation volume lies within the rib tip. The simulation has not been carried out right to the walls, but a similar effect to that seen in figure 4 will occur. Note that the simulation produces data in the centre of the channel, even though the measurement plane is inside the rib at this point.

6. Experimental results

Velocity profiles were obtained at five evenly spaced heights within the straight channel. By using 640×8 pixel interrogation spots and averaging over 100 image pairs a resolution of $212 \times 2.64 \times 13.3 \mu\text{m}$ is obtained. The out-of-plane resolution of $13.3 \mu\text{m}$ is taken as $2z_{\text{corr}}$ and corresponds to the depth over which particles produce a significant contribution to the correlation function [9]. The large spot length is possible without introducing significant error because the flow is unchanging along the channel. Analysis of the scatter in data from 1000 image pairs suggests that averaging the correlation function arithmetically over 100 image pairs converges u_{PIV} to within 2% of u_{PIV}^* . Sources of this error include fluctuations due to Brownian motion of the particles, particle distribution within the interrogation volume and the locating of the particle image centres. In addition, there are errors associated with the determination of the experimental parameters. The applied pressure gradient is estimated as accurate to within 1% and the channel dimensions to around 1.4% in the isotropically etched channel. Combining these errors leads to an overall 3% random error in the measured velocity. This is clearly dominant over the systematic difference of 0.7% between u_{PIV}^* and u_0 .

A comparison between u_0 and u_{PIV} on the $z = 0.60$ plane is shown in figure 6. The computations have been made predictively using the pressure heads in the reservoirs and the measured channel dimensions and the experimental results have not been fitted to them. The shapes of the two profiles are similar, although a skewness is apparent. u_{PIV} is below u_0 as expected (see figure 4), with the deviation in the centre of the channel being 1.4% of the mean velocity. This is larger than the 0.7% predicted by the micro-PIV simulations, although still within the experimental error of 3%. The results on the other planes show similar trends.

In the ribbed channel, results were obtained on three horizontal planes at different depths in the channel. Averaging over 80 images allowed a 64×64 pixel grid size to be used. This corresponds to a $21.2 \times 21.2 \mu\text{m}$ interrogation spot compared to a device width of $510 \mu\text{m}$. The depth of correlation is again $13.3 \mu\text{m}$, which is 29% of the channel

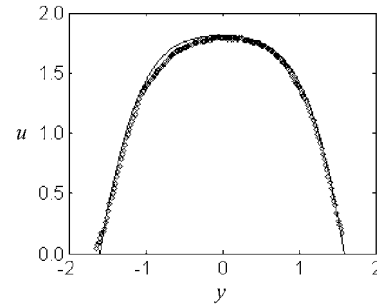


Figure 6. Velocity profiles at $z = 0.60$ in the straight channel. The solid line is u_0 and the diamonds are the experimental micro-PIV results, u_{PIV} . The results differ by around 1.4% in the centre compared to an experimental uncertainty of 3%, with a significant skewness on the left-hand side. The results at other heights show similar trends and are not plotted here.

depth. Two of the measurement planes lie in the main channel and one is near the tip of the ribs. Again, the correlation averaging should converge u_{PIV} to within around 2% of u_{PIV}^* . However, in the ribbed channel the uncertainty in the geometric parameters is greater. In particular the ratio h/R (figure 3) is difficult to determine, and is estimated as being accurate to around 10%. Thus, whilst the systematic differences are larger in the ribbed channel (see figure 5), the experimental uncertainties should still dominate the comparison between u_{PIV} and u_0 .

Figure 7 shows vector plots for two of the three planes. The flow angle adjusts in a similar way at all depths, with the turn across the ribs particularly noticeable. The low velocities around the ribs on the $z = 0.68$ plane is a result of the proximity of the roof of the channel as it curves down to the rib tip. The fluid motion will also have a more significant z component at this point, which cannot be determined from the two-dimensional technique used here. No filtering has been applied to the vectors, which were obtained by arithmetically averaging the correlation functions from 80 image pairs.

Figure 8 shows comparisons of the u and v velocity along the y axis with the CFD results. Difficulties in obtaining an accurate pressure—mass flowrate characteristic means that the flow rate in the computations has been adjusted to fit the maximum u_{PIV} on plane $z = 0.68$. The adjusted flow rate is, however, the same on all measurement planes and for both velocity components. In fact u_{PIV} should be slightly below u_0 in an ideal set of data (figure 5). There is general agreement between the shape of the experimental and theoretical results, with the majority of the deviations lying within the errors expected due to the 10% geometrical uncertainty. Note that the results are along the y axis (figure 3) and therefore will not necessarily exhibit periodicity on either side of the rib. Significant deviations are noticeable at low y on the $z = 0.68$ plane. As predicted by the simulations (figure 5), data have also been obtained in the centre of this plane even though at this point the centre of the interrogation spot lies inside the rib in the roof of the channel.

7. Discussion

The systematic deviation between u_{PIV}^* and u_0 depends on the second spatial derivative of velocity and the size of the

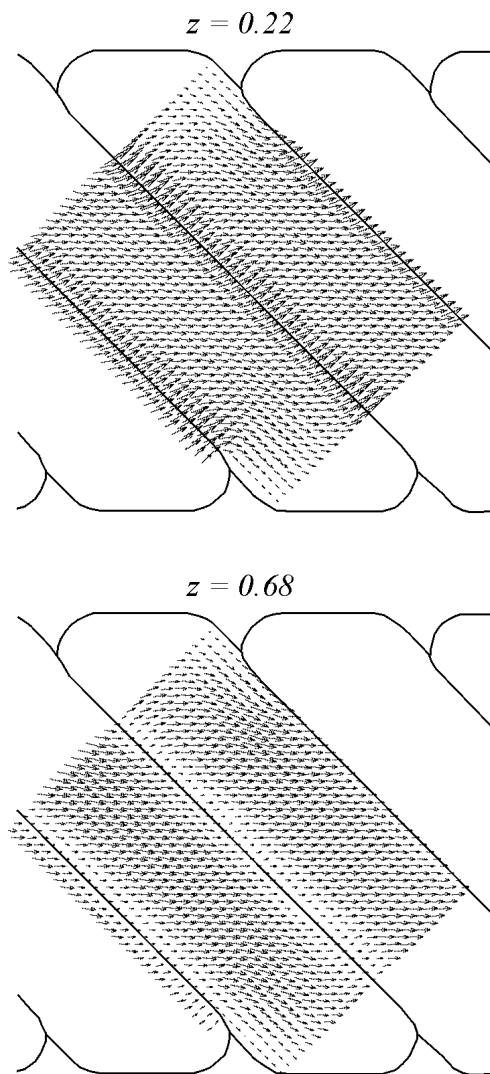


Figure 7. Velocity vectors in the ribbed microchannel. Vectors are obtained from a correlation average over 80 image pairs and have not been filtered. The vector scale is the same for both measurement planes so direct comparison is possible. The outline shown is the position of the ribs and the base of the channel, the curvature of the walls means that the edges of the channel will be inside this outline at larger z . The results on the $z = 0.46$ plane are similar to those on the $z = 0.22$ plane and are not shown. The rib tip is at $z = 0.55$.

interrogation spot. In the isotropically etched, straight channel (figure 4) the deviation is small because there are no large changes in velocity gradient. The deviation is greatest in the centre of the channel ($y = 0$) where the second derivative, $\partial^2 u_0 / \partial z^2$ is largest. However, even here the deviation is only 0.7% of the mean fluid velocity. Also, the fourth derivative is approximately zero over most of the channel, so the approximation in equation (6) is a good one in this case. In the ribbed channel the second derivatives are larger and thus the spots, whilst smaller in area, contain greater variations in velocity gradient. This is particularly true near the ribs, where second velocity derivatives are largest. This explains why the deviation between \mathbf{u}_{PIV}^* and \mathbf{u}_0 is greater in the ribbed channel (figure 5), and demonstrates the possibility of tailoring the shape of the interrogation spot to the flow in question.

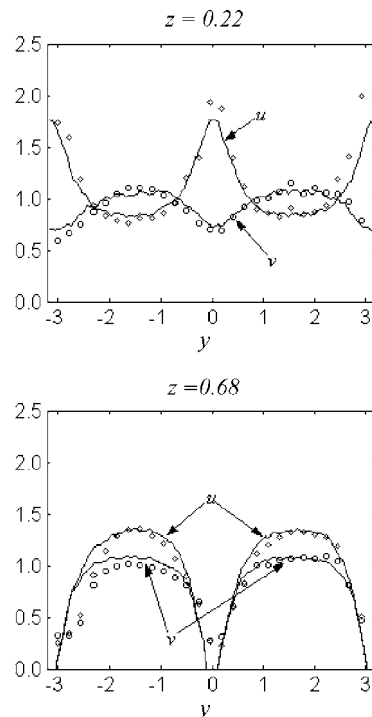


Figure 8. Velocity profiles along the y axis in the ribbed channel. The solid lines represent u_0 and v_0 at the measurement plane, whilst the u_{PIV} and v_{PIV} results are shown with diamonds and circles respectively. The total flowrate has been fitted to the experimental data but separate adjustments have not been made on individual planes. The $z = 0.46$ profile is similar to that at $z = 0.22$ and is not shown.

In both cases, however, the systematic deviation is outweighed by the experimental uncertainties arising from the micro-PIV technique and the determination of the experimental parameters. In the straight channel the total uncertainty is estimated at 3% of the mean velocity, compared to a systematic deviation of just 0.7%. Also, the skewness that is apparent in figure 6 suggests unevenness in the etching in addition to the error in the determination of the channel depth and width. Similarly, in the ribbed channel the dominating error is again likely to be the uncertainty in geometric parameters. In particular the ratio h/R (figure 3) is estimated as being accurate to around 10%. The fact that v_{PIV} tends to be lower than v_0 in the grooves and higher across the rib tip ($y = 0$ in figure 8), whilst the opposite applies to u , suggests that the flow is actually snaking more than expected. This is likely to be because the ribs actually extend further into the channel than the five parameter model used to generate the computational geometry places them. The significant deviation at low y on the $z = 0.68$ measurement plane is also likely to be the result of an uneven etching of the rib at that point. The systematic errors associated with velocity variation over the interrogation volume are larger for the ribbed channel than for the straight channel, around 7.5% of the mean velocity whilst the interrogation spots are entirely within the flow (figure 5). However, the dominating factor in the comparison between the micro-PIV results and CFD simulations is not the spatial resolution of the experimental data, but remains the precision with which the experimental parameters can be determined. This highlights that, whilst

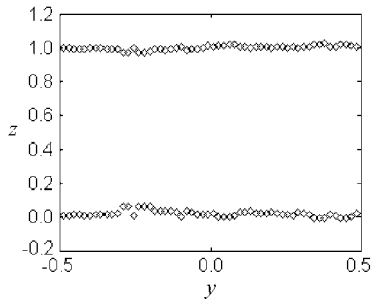


Figure 9. Positions of the top and bottom walls across the centre of the straight microchannel.

improving the resolution of the micro-PIV data will reduce the systematic deviation, if the experimental uncertainties are the dominating source of error this may not in itself improve the overall accuracy of the experiment.

In both experimental cases there are examples of results being obtained when the centre of the interrogation spot lies in the channel walls. Particularly noticeable is that results are obtained $4.7 \mu\text{m}$ beyond the channel edge even though the spot width is only $2.6 \mu\text{m}$ (figure 4). The tendency for the experimental results to curve up at the edges is clear in figure 6. This is because the curved walls of the channel and the depth of the interrogation volume mean that data can be obtained from below the measurement plane, where the channel is wider, even when the centre of the volume is in the wall. If accurate data are to be obtained close to surfaces that are not perpendicular to the image plane it will be very important to restrict the depth of the interrogation volume. This can be achieved by using lenses with a low n/NA ratio.

It is particularly difficult to determine the z location of the micro-PIV measurement plane and the depth of the channel. Near the top and the bottom of the channel, a 1% error in locating the measurement plane results in a 10% error in the measured velocity. The principal source of error when making z measurements is associated with establishing a reference location. Focusing by eye on points within the channel to determine the reference location is estimated to be accurate to within about $3 \mu\text{m}$. By contrast the relative displacement between planes can be determined to within $0.4 \mu\text{m}$, the accuracy of the stage translation. The micro-PIV results can be used to improve the accuracy with which the reference location is determined. First, CFD simulations are used to identify areas in which the flow is parabolic in the z direction. Then, micro-PIV profiles of u versus z are obtained using data from all five measurement planes. A parabolic profile can be fitted to the micro-PIV data and the position of the top and bottom surfaces determined from the zero points of the parabola. The technique is applied in the centre part of the straight channel, where the profile is parabolic, and has been used in this study to provide the channel depth R for the CFD computations and the $z = 0$ reference location for the experimental data. In the centre of the ribbed channel grooves the flow is also closely parabolic and thus R and $z = 0$ can also be determined in this way in the ribbed channel. Figure 9 shows a series of depth measurements versus y position across the straight channel, whilst figure 10 shows similar results versus x along the centre

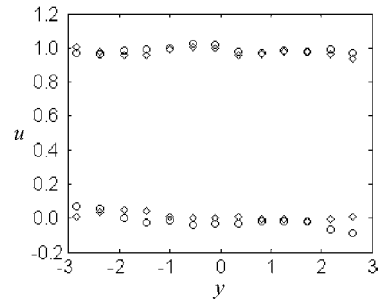


Figure 10. Positions of the top and bottom walls along the centre of two adjacent grooves of the ribbed microchannel. The circles are the first groove and the diamonds are the second.

of the grooves of the ribbed channel. The uncertainty in the mean position of the straight channel top and bottom when averaged over many interrogation volumes across the centre of the channel is just $0.2 \mu\text{m}$, which is comparable to the uncertainty in plane spacing and a significant improvement on measurements made by eye. Similarly, in the ribbed channel the mean position of the surfaces can be determined to within $0.4 \mu\text{m}$.

8. Conclusion

A methodology has been presented for predicting micro-PIV velocities from CFD flow simulations. The method applies the relations developed to define the depth of correlation [9, 11] and the optical properties of infinity corrected lens systems [7] to produce the required weighted average across interrogation volumes within the CFD solution. Providing the in-plane resolution is sufficiently small, the systematic error between the micro-PIV velocity and the fluid velocity at the centre of the interrogation spot depends principally on the interrogation volume depth and the second derivative of the fluid velocity with respect to z . In more complex flows higher even derivatives of the fluid velocity may also be important.

In the straight, isotropically etched channel used in these experiments, the maximum systematic error resulting from the variation of velocity within the interrogation volume is found to be 0.7% of the centreline velocity for the lens system used ($M = 20, \text{NA} = 0.4$). This is small compared to the experimental errors relating to the micro-PIV technique and measurement of the applied pressure gradient and the channel geometry, which, in total, are estimated at 3% of the centreline velocity.

In the interference etched channel the flow is more complex and hence the systematic deviations are larger. In the centre of the grooves the error is still of the order of 1% of the centreline velocity of an equivalent isotropically etched channel. Near the ribs this rises to around 7.5% for interrogation volumes completely within the fluid and up to 20% when the volumes are partially within the solid wall. At the same time, however, the more complex channel shape results in greater geometric uncertainty and the experimental errors still dominate the results.

Thus the quality of the comparison between CFD and micro-PIV data, for the experiments here, appears to depend principally on the determination of the experimental parameters and not on the resolution of the micro-PIV data.

This means that if a large field of view or large depth of correlation is required, or if poor optical access means that high NA lenses are impractical, lens systems with higher n/NA ratio can be used without reducing the quality of the comparison.

An exception to this is where data are required very close to a wall that is not perpendicular to the measurement plane. Systematic errors occur close to the walls due to part of the interrogation volume remaining in the flow when the centre is actually in the channel wall. Evidence of this effect is found in the experimental profiles obtained. For the case of the straight channel, the CFD simulations predict that experimental data can be obtained up to $4.7\ \mu\text{m}$ outside of the channel even though the interrogation spots are only $2.6\ \mu\text{m}$ wide. This suggests that the depth of correlation is the controlling factor. To avoid this effect the depth of correlation of the measurements must be reduced and low n/NA lens systems are therefore required.

Another important source of experimental error is found to be the location of the measurement plane in the z direction. A technique involving parabolic fitting of u versus z micro-PIV data to determine the positions of the top and bottom surfaces of the channels has been presented. The technique has been demonstrated to be accurate to within $0.2\ \mu\text{m}$, 15 times more accurate than estimations made by eye. It can be used to provide accurate measurements of the depth of microfluidic devices.

References

- [1] Koutsiaris A G, Mathioulakis D S and Tsangaris S 1999 Microscope PIV for velocity-field measurement of particle suspensions flowing inside glass capillaries *Meas. Sci. Technol.* **10** 1037–46
- [2] Meinhart C D, Wereley S T and Santiago J G 1999 PIV measurements of a microchannel flow *Exp. Fluids* **27** 414–9
- [3] Meinhart C D and Zhang H 2000 The flow structure inside a microfabricated inkjet printhead *J. Microelectromech. Syst.* **9** 67–75
- [4] Wereley S T, Meinhart C D, Santiago J G and Adrian R J 1998 Velocimetry for MEMS applications *MEMS, ASME (Anaheim, CA)*
- [5] Klank H, Goranovic G, Kutter J P, Gjelstrup H and Michelsen J 2002 PIV measurements in a microfluidic 3d-sheathing structure with three dimensional flow behaviour *J. Micromech. Microeng.* **12** 862–9
- [6] Wu Z, Truong T-Q, Nguyen N-T and Huang X-Y 2003 Characterisation of microfluidic devices using micro particle image velocimetry *Int. J. Comput. Eng. Sci.* **4** 269–72
- [7] Meinhart C D and Wereley S T 2003 The theory of diffraction limited resolution in microparticle image velocimetry *Meas. Sci. Technol.* **14** 1047–53
- [8] Meinhart C D, Wereley S T and Gray M H B 2000 Volume illumination for two-dimensional particle image velocimetry *Meas. Sci. Technol.* **11** 809–14
- [9] Olsen M G and Adrian R J 2000 Out-of-focus effects on particle image visibility and correlation in microscopic particle image velocimetry *Exp. Fluids (Suppl.)* S166–74
- [10] Olsen M G and Adrian R J 2000 Brownian motion and correlation in particle image velocimetry *Opt. Lasers Technol.* **32** 621–7
- [11] Olsen M G and Bourdon C J 2003 Out-of-plane motion effects in microscopic particle image velocimetry *J. Fluids Eng.* **125** 895–901
- [12] Bourdon C J, Olsen M G and Gorby A D 2004 Validation of an analytical solution for depth of correlation in microscopic particle image velocimetry *Meas. Sci. Technol.* **15** 318–27
- [13] Devasenathipathy S, Santiago J G, Meinhart C D and Takehara K 2003 Particle imaging techniques for microfabricated fluidic systems *Exp. Fluids* **34** 504–14
- [14] Prasad A K, Adrian R J, Landreth C C and Offut P W 1992 Effect of resolution on the speed and accuracy of particle image velocimetry interrogation *Exp. Fluids* **13** 105–16
- [15] MacInnes J M, Du X and Allen R W K 2003 Prediction of electrokinetic and pressure flow in a microchannel T-junction *Phys. Fluids* **11** 1992–2005
- [16] Tretheway D C and Meinhart C D 2003 Effects of absolute pressure on fluid-slip in a hydrophobic microchannel *IMECE 2003 (ASME)*
- [17] Westerweel J 1997 Fundamentals of digital particle image velocimetry *Meas. Sci. Technol.* **8** 1379–92